Available online at www.sciencedirect.com
ScienceDirect
Trans. Nonferrous Met. Soc. China 32(2022) 3699−3713
Transactions of Nonferrous Metals Society of China
www.tnmsc.cn

Failure modes and slabbing mechanisms of hard rock with different height-to-width ratios under uniaxial compression

Yu-zhe ZHAO[1], Lin-qi HUANG[1], Xi-bing LI[1], Chong-jin LI[1], Zheng-hong CHEN[2], Zhi-wei CAO[1]

1. School of Resources and Safety Engineering, Central South University, Changsha 410083, China;
2. School of Civil Engineering, Hunan University of Science and Technology, Xiangtan 411201, China

Received 15 August 2021; accepted 4 March 2022

Abstract: To determine the relationship between slabbing failure and the specimen height-to-width (H/W) ratio and to analyze the conditions, characteristics, and mechanism of slabbing failure in the laboratory, uniaxial compression tests were conducted using six groups of granite specimens. The entire failure process was recorded using strain gauges and high-speed cameras. The initiation and propagation of fractures in specimens were identified by analyzing the monitoring results of stress, strain, and acoustic emission. The experimental results show that changes in the specimen H/W ratio can transform the macro failure mode. When the H/W ratio is reduced to 0.5, the macro failure mode is dominated by slabbing. Low load-bearing ability is observed in specimens with slabbing failure, and the slabbing fractures are approximately parallel to the loading direction. Moreover, the fracture propagation characteristics and acoustic emission signals of slabbing failure specimens show typical tensile failure characteristics, indicating that slabbing failure is essentially a special tensile failure.

Key words: hard rock; failure mode; slabbing failure; acoustic emission; tensile wing fracture

1 Introduction

With the increasing demand for mineral resources and the consumption of shallow resources, an increasing number of hard rock mines encounter deep mining conditions [1]. In deep mining, slabbing (or spalling) failure occurs in hard rock rather than shear failure under high-stress conditions [2−5]. FAIRHURST and COOK [6] provided a detailed description of the slabbing failure. ORTLEPP [7] conducted a detailed study on slabbing fracture damage and defined slabbing as a formation of stress-induced slabs on the boundary of an underground excavation. CAI [8] found that onion-skin-type fractures were densely distributed in the surrounding rock of a cave where the slabbing failure occurred. In addition to the surrounding rock of the cave, slabbing failure was also observed in the hard rock pillar [9]. MARTIN and MAYBEE [10] investigated 178 hard rock pillars in Canadian mines. Their results showed that the strength of pillars with slabbing failure was much lower than the design strength. Thus, it is necessary to investigate the failure mode and mechanism of slabbing, especially in short pillars, and to propose a reliable strength calculation method.

Generally, pillars in underground mines and surrounding rock at the intersection of underground crossed roadways are under uniaxial stress [11], similar to rock specimens under uniaxial compression. Many researchers have conducted uniaxial compression tests on rock specimens to reproduce the stress conditions of the pillar to study the strength and slabbing failure [12,13]. But compared with shear failure, slabbing was rarely observed in conventional uniaxial compression

Corresponding author: Lin-qi HUANG, Tel: +86-13469059806, E-mail: huanglinqi@csu.edu.cn
DOI: 10.1016/S1003-6326(22)66050-3

experiments. Several studies used the specimens containing pre-manufactured initial defects to investigate the slabbing failure further, and the relationship between microscopic defects and slabbing failure has been revealed [14,15]. Apart from rock specimens with pre-manufactured initial defects, slabbing failures were also reported in intact specimens with low slenderness ratios (length-to-diameter ratio or height-to-width ratio) in uniaxial compression tests [16,17].

However, there are no unified conclusions regarding the effects of the specimen slenderness ratio under uniaxial compressive conditions. From previous studies of intact cylindrical and prismatic rock specimens under compression, the main findings regarding the slenderness ratio effect are summarized as follows.

(1) Many previous studies have concluded that uniaxial compressive strength (UCS) increases with a decrease in slenderness ratio [18−25]. However, there are different conclusions presented in other studies. The results of THURO et al [26] show that the UCS of specimens with a length-to-diameter (L/D) ratio of 1.0 decreased somewhat compared to specimens with an L/D ratio of 1.2. LI et al [16] found that the UCS of prism specimens decreased when the specimen H/W ratio decreased to 0.5. They indicated that the decrease in UCS was due to the slabbing failure. However, it should be noted that in Ref. [16], only three groups of specimens (H/W ratios are 2.4, 1.0, and 0.5, respectively) have been tested, and only in one group (H/W ratio is 0.5), the slabbing failure is observed. Relatively few specimen groups with different H/W ratios were difficult to describe the influence of the H/W ratio on the UCS accurately. WEN et al [27] indicated that the post-peak mechanical properties were more complicated when the L/D ratio of the specimen was less than 1.0. Thus, there is controversy regarding the relationship between the UCS and the slenderness ratio when the L/D ratio or H/W ratio of specimen is relatively low. Regarding the UCS of specimens with a low H/W ratio, especially those with a H/W ratio less than 1.0, further research on more experimental specimen groups is needed.

(2) Some scholars believe that slenderness ratio effects result from the friction constraint caused by the end effect; the end of the specimen is in a triaxial stress state due to the action of the friction force. The proportion of the triaxial stress zone in the specimen increases as the slenderness ratio decreases, resulting in an increase in the UCS [28−30]. Moreover, some scholars believe that slenderness ratio effects are related to the volume of the specimen. As the slenderness ratio decreases, the specimen volume becomes smaller, and the distribution probability of microscopic defects decreases. Thus, the UCS increases [31−34]. To some extent, both theories explain why the UCS increases with decreasing slenderness ratio. Unfortunately, neither of these theories can explain the sudden decrease in the UCS at relatively low slenderness ratios.

(3) According to previous studies, the failure mode is affected by the slenderness ratio of the specimen. Generally, the failure mode is considered to be shear in the uniaxial compression test when using standard specimens with specified slenderness ratios. A series of classical shear failure criteria have been proposed to explain the shear failure of rock specimens [35−39]. However, some uniaxial compression test results show different failure modes. Instead of shear failure, slabbing failures were observed in short specimens under uniaxial compression [40−42]. Thus, the failure modes of specimens with relatively low slenderness ratios require further investigation to explain the slabbing failure of short pillars in practical engineering.

Although the slenderness ratio effect in uniaxial compression conditions has been analyzed in many previous studies, most of them focused on the UCS (uniaxial compressive strength), and discussion on the failure modes was limited, such as LI et al [16]. The decrease in the UCS is only an intuitive phenomenon when the failure mode is dominated by slabbing failure. The underlying mechanical mechanism needs further discussion. Moreover, the mechanical behaviors of specimens with relatively low H/W ratios were not fully considered. The main focus was the UCS in previous studies, and the failure modes were often not considered. In particular, the slabbing failure in specimens with low H/L ratios (<1.0) has rarely been investigated; the slabbing failure mechanism is unclear. Therefore, in this study, uniaxial compression tests were conducted on granite specimens with different H/W ratios to determine the relationship between the H/W ratio and the failure mode and to analyze the mechanism of

slabbing failure. During the uniaxial compression tests, acoustic emissions were monitored to detect the fracture initiation and propagation, strain monitoring points were set to log the local deformation, and a high-speed camera was used to record the entire failure process.

2 Experimental

2.1 Specimen preparation

Miluo granite, a typically hard and brittle rock sourced from Hunan Province, China, was used in this study. All tested granite specimens were obtained from a large and integral granite block to ensure homogeneity among the specimens. Six H/W ratios were considered in this study; there were six groups of specimens with different geometric shapes, as shown in Fig. 1.

Group A: height × width × thickness: 200 mm × 100 mm × 50 mm, with a specimen H/W of 2.0; Group B: height × width × thickness: 100 mm × 100 mm × 50 mm, with a specimen H/W of 1.0; Group C: height × width × thickness: 75 mm × 100 mm × 50 mm, with a specimen H/W of 0.75; Group D: height × width × thickness: 50 mm ×100 mm × 50 mm, with a specimen H/W of 0.50; Group E: height × width × thickness: 35 mm × 100 mm × 50 mm, with a specimen H/W of 0.35; Group F: height × width × thickness: 20 mm × 100 mm × 50 mm, with a specimen H/W of 0.20.

Groups A, B, C, and D were prepared with three specimens in each group; Groups E and F were prepared with four specimens. The average density of the tested granite specimens was 2623.14 kg/m^3. To minimize end effects during the experiments, all six surfaces of the specimens were polished carefully using a grinding machine to produce smooth end surfaces and good perpendicularity. Furthermore, the lubricant (prepared by placing stearic acid crystals and Vaseline) was applied to the top and end surfaces of the specimen to reduce the friction between the specimen and platens. All tests were performed on dry rock specimens at room temperature.

2.2 Test apparatus

The test apparatus is shown in Fig. 2, consisting of four parts: a servo-hydraulic rock mechanics testing system (Instron−1346), an acoustic emission (AE) monitoring system, a strain

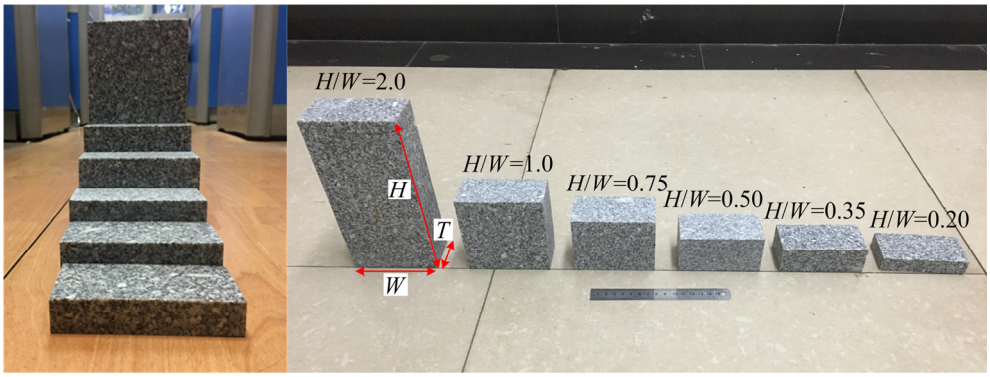

Fig. 1 Six groups of granite specimens with different H/W ratios used in experiment

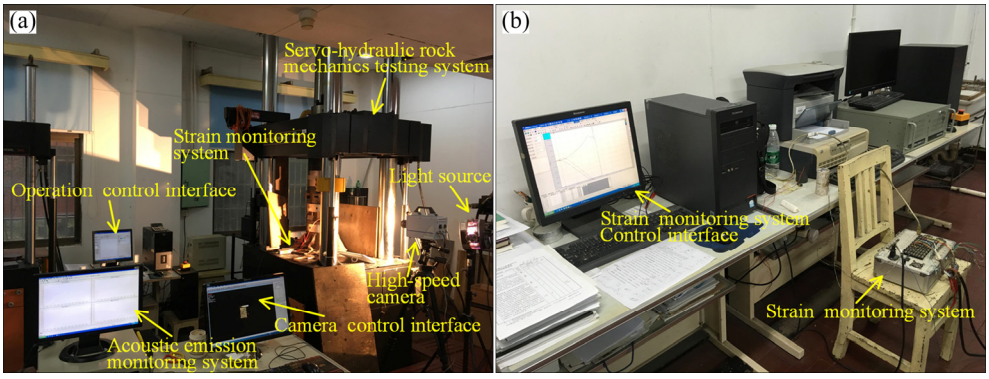

Fig. 2 Photographs of test system: (a) Servo-hydraulic rock mechanics testing system, AE monitoring system and high-speed camera system; (b) Strain monitoring system

monitoring system, and a high-speed camera system (FASTCAM SA 1.1). The servo-hydraulic rock mechanics testing system had a maximum axial loading capacity of 2000 kN, with a load measurement accuracy of ±0.5%. The AE monitoring system used PCI−2 acoustic emission monitoring equipment. The strain monitoring system was set to monitor local deformation. A high-speed camera system was used to record the entire failure process in the experiment, and the frame frequency of the high-speed camera was set to 125 frame/s.

2.3 Test procedure

Prior to the uniaxial compression tests, strain gauges (Model BX120 5BA) were attached to the rock specimens to monitor the horizontal and vertical strains at each monitoring point, as shown in Fig. 3(a). The specimens in Groups A and B were arranged with three points for strain monitoring, and the specimens in Groups C, D, E, and F were arranged with two points for strain monitoring due to the limited specimen height. All specimens were instrumented with two AE monitoring probes at the center; the high-speed camera was aimed at the specimens, as shown in Fig. 3(b).

In the uniaxial compression tests, an axial force was imposed on the specimen ends under force-controlled conditions with a constant vertical loading speed of 120 kN/min for 2 min to cause the specimen end to contact the testing machine. The axial force control conditions were changed to displacement control conditions with a loading speed of 0.065 mm/min until failure occurred, and a linear variable differential transformer (LVDT) was used to measure the evolution of the axial deformation of the specimens.

3 Results

3.1 Stress−strain curves

The stress−strain curves of the uniaxial compression tests are illustrated in Figs. 4(a−f) for specimens with H/W ratios of 2.0, 1.0, 0.75, 0.50, 0.35 and 0.20, respectively. The stress−strain curves of all specimens showed similar plastic compaction characteristics in the early loading phase. However, the curves exhibit significant differences in the yield phase for different H/W ratios. For Groups A and B, with H/W ratios greater than or equal to 1.0, the stress−strain curves do not fluctuate significantly during the peak phase, indicating that the failure process in the peak phase undergoes a short plastic deformation phase before brittle failure occurs. For Groups C, D, E, and F, with H/W ratios less than 1.0, a long fluctuation region in the peak

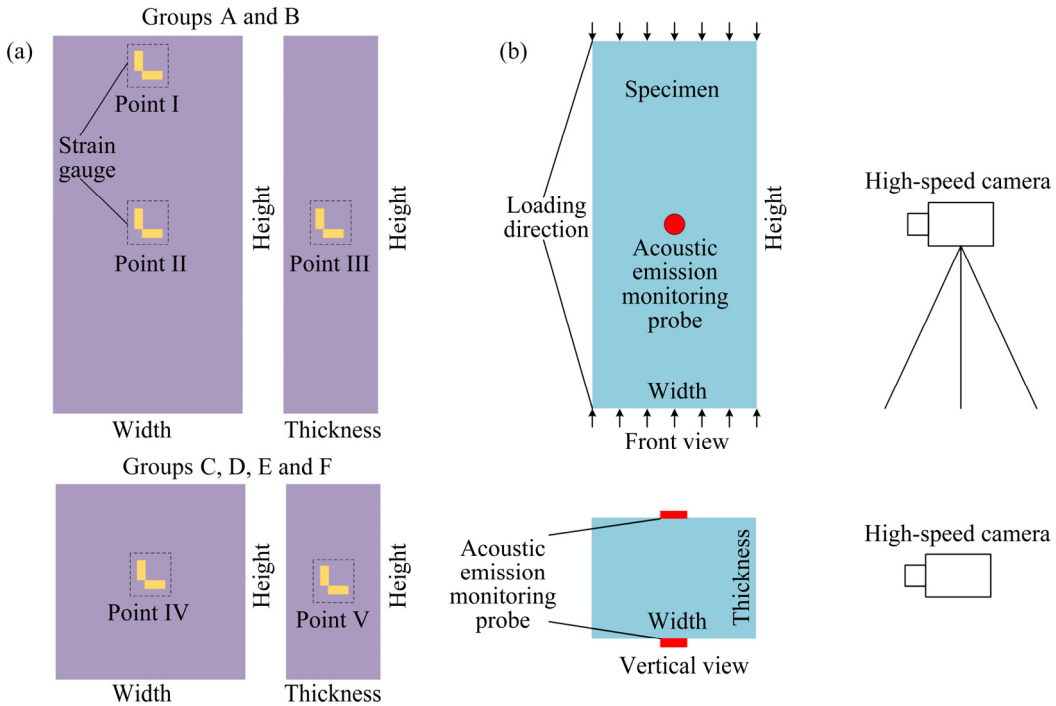

Fig. 3 Schematic diagrams of experimental equipment layout: (a) Strain monitoring points; (b) AE monitoring probe and high-speed camera

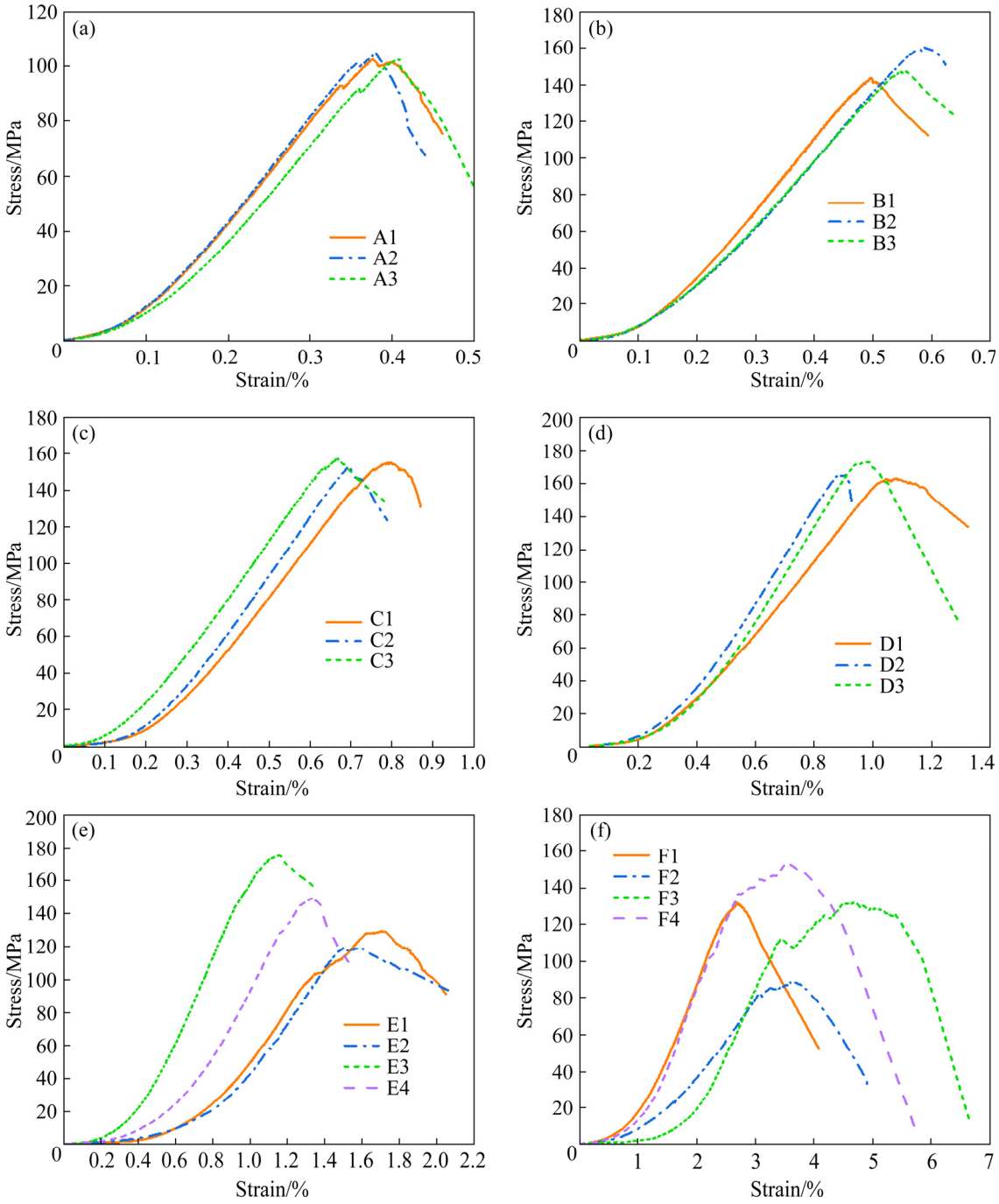

Fig. 4 Stress−strain curves of specimens with different H/W ratios: (a) Group A (H/W=2.0); (b) Group B (H/W=1.0); (c) Group C (H/W=0.75); (d) Group A (H/W=0.50); (e) Group E (H/W=0.35); (f) Group F (H/W=0.20)

phase gradually appears in the stress−strain curves as the H/W ratio decreases, especially for specimens in Group F. In the fluctuation region, the stress increases slowly with the increase of the strain and undergoes irregular oscillation to the peak value because slabbing fractures occur early in the uniaxial compression process for specimens with low H/W ratios. Because the slabbing fractures are parallel to the maximum loading direction, the specimen can sustain further stress after some slabbing fractures have formed, indicating that specimens with low H/W ratios experience a long plastic failure process between the onset of slabbing fractures and complete failure.

The average peak strain of specimens in Group A (H/W=2.0) is approximately 0.388%; the average peak strain is 3.559% in Group F (H/W=0.2), 8 times greater than in Group A. The increase in peak

strain with a decrease in the H/W ratio indicates that severer plastic deformation occurs in specimens with low H/W ratios. The failure process changes from elastic-brittleness to elastic-plasticity with a decrease in the H/W ratio.

The average peak stress firstly increases and then decreases as the H/W ratio decreases.

3.2 Failure mode

As shown in Fig. 5, different H/W ratios produce different failure modes in uniaxial compression tests.

Fig. 5 Typical failure results of some specimens in Groups A (a−d), B (e−h), C (i−l), D (m−p), E (q−t) and F (u−x)

For Groups A and B ($1.0 \leq H/W \leq 2.0$), shear fractures dominate the specimen failures. Only one or two shear fractures are observed on the lateral wall of the specimen, indicating that shear fractures connect to each other during uniaxial loading, eventually forming one or two main shear planes (Figs. 5(b, f)). The failure of specimens is brittle, transient, and the same as that of a cylindrical specimen with a high H/L ratio. Photographs of specimen residues show that the remaining specimen pieces have a triangular-cone shape (Figs. 5(d, h)), confirming that the specimen failure is dominated by shear.

For Groups C and D ($0.5 \leq H/W < 1.0$), the specimen failure is controlled by shear and slabbing. The lateral and top views of the specimens in Groups C and D indicate more shear fractures than Groups A and B. Moreover, obvious slabbing fractures appear on the specimen surfaces, and the slabbing fractures increase with a decrease in the H/W ratio.

For Groups E and F ($H/W < 0.5$), slabbing fractures dominate the failures of specimens. The lateral views clearly show multiple sets of slabbing fractures on the specimen surfaces nearly parallel to the loading direction. The specimen is divided into many thin flake fragments by numerous closely arranged parallel slabbing fractures (Figs. 5(s, x)). In addition, exfoliation is observed on the part of the specimen surface (Figs. 5(u, v)). When the H/W ratio increases from 0.35 to 2.0, the angle of the macro-fracture plane (the angle between the normal of the fracture plane and the axial direction) decreases from approximately 90° to approximately 70°, and the number of fractures significantly decreases.

Comparing the typical failure modes of specimens in Groups A, B, C, D, E and F, it is observed that the specimen failure gradually changes from shear to slabbing with a decrease in the H/W ratio.

3.3 Failure process

There are obvious differences in the failure processes of specimens with different H/W ratios. The failure processes of specimens in uniaxial compression tests were recorded using a high-speed camera. To analyze the effect of failure mode on the failure process, a series of photographs and the stress−strain curves of three typical specimens with different failure modes (shear failure, shear–slabbing mixed failure, and slabbing failure) are shown in Fig. 6.

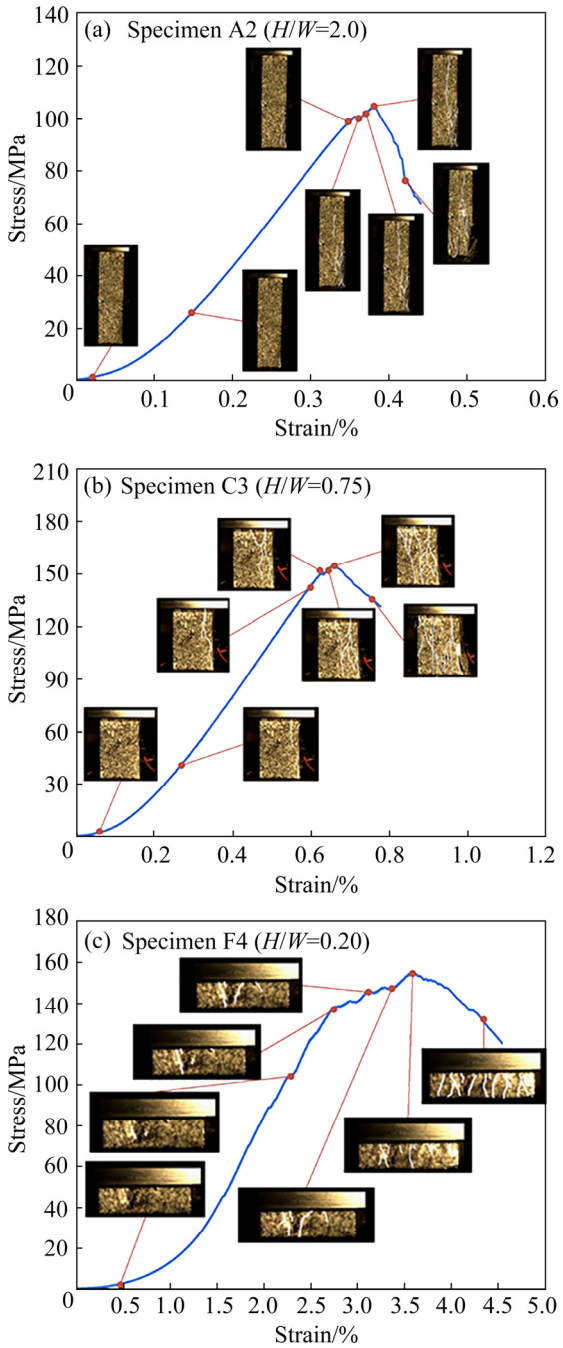

Fig. 6 Stress−strain curves and failure process of specimens in shear failure (a), shear−slabbing mixed failure (b) and slabbing failure (c)

For Specimen A2, the failure process was controlled by shear failure. The first macro visible fracture occurred in the yield phase of the uniaxial compression process, indicating the late occurrence of fractures in the failure process. The fractures

expanded rapidly, and the specimen underwent a short yield process before suffering a significant brittle failure. The failure process was transient and brittle, and a single complete shear failure plane was formed.

For Specimen C3, the failure process was controlled by shear–slabbing mixed failure. The failure process is of elastic-plastic characteristics. Local fractures appeared in the specimen before the yield phase, but no complete failure plane was formed. The number of fractures increased, and local slabbing fractures appeared on the specimen surface during the yield phase.

For Specimen F4, the failure process was controlled by slabbing failure. The failure process indicates significant plastic characteristics. The specimen had a short elastic phase and a long plastic yield phase. The slabbing fracture firstly appeared at the center of the specimen, gradually forming slabbing failure planes. Because the fractures were parallel to the maximum loading direction, the specimen could sustain further stress. As loading continued, more slabbing fractures appeared, expanding to form new slabbing failure planes. After a long plastic yield phase, the specimen was finally cut into thin flake fragments by many parallel slabbing failure planes.

The failure process of the specimen gradually changes with a decrease in the H/W ratio, and the yield phase of the specimen gradually becomes longer. More parallel fractures are generated and expanded during the yield phase, and the fracture angle gradually becomes parallel to the loading direction. The fracture distribution gradually changes from concentrated to discrete.

4 Discussion

4.1 Influence of H/W ratio on uniaxial compression strength

The UCS is an important indicator for analyzing the failure modes of specimens with different H/W ratios. To investigate the influence of the H/W ratio on the UCS of specimen, the relationship between the UCS and the H/W ratio is discussed.

Many previous experiments have shown that the UCS increased with a decreasing slenderness ratio (L/D ratio or H/W ratio), and have indicated that the increase in the UCS was caused by the end effect [43]. However, our experimental results present that the UCS does not always increase with a decrease in the H/W ratio, decreasing when the H/W ratio is less than 0.50 (as shown in Fig. 7). The change in the UCS is not only affected by the end effect, but also by the failure mode of the specimen. When the H/W ratio of the specimen is less than 0.50, the failure mode changes from shear failure to slabbing failure; most previous experiments did not consider such a low H/W ratio. Because the slabbing failure is controlled by the tensile stress and the tensile strength of the rock itself is much less than the compressive strength, slabbing fracture occurs quickly, leading to rapid destruction. The UCS of a granite prism specimen increases first and then decreases with a decrease in the H/W ratio.

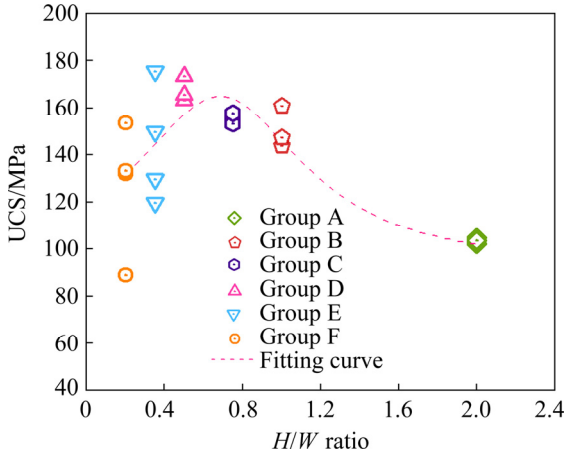

Fig. 7 Variation of UCS with H/W ratio for six groups of prism specimens

When the H/W ratio of the specimen is less than 0.50, the UCS in the same group is more discrete because the specimen is thinner and more sensitive to initial defects. High UCS discreteness in relatively low H/W ratio specimens was also reported in previous experiments [16,20].

4.2 Influence of H/W ratio on strain

To deeply analyze the local strain changes in different parts of the specimen, monitoring points were set for strain detection at different locations on the specimen (as shown in Fig. 3). The obtained strain−time curves for specimens with different H/W ratios are shown in Fig. 8. The strain−time curves of each monitoring point reveal different variation rules with changes in the specimen H/W ratio. For specimens with a H/W ratio greater than 1.0, the horizontal and vertical strains at monitoring

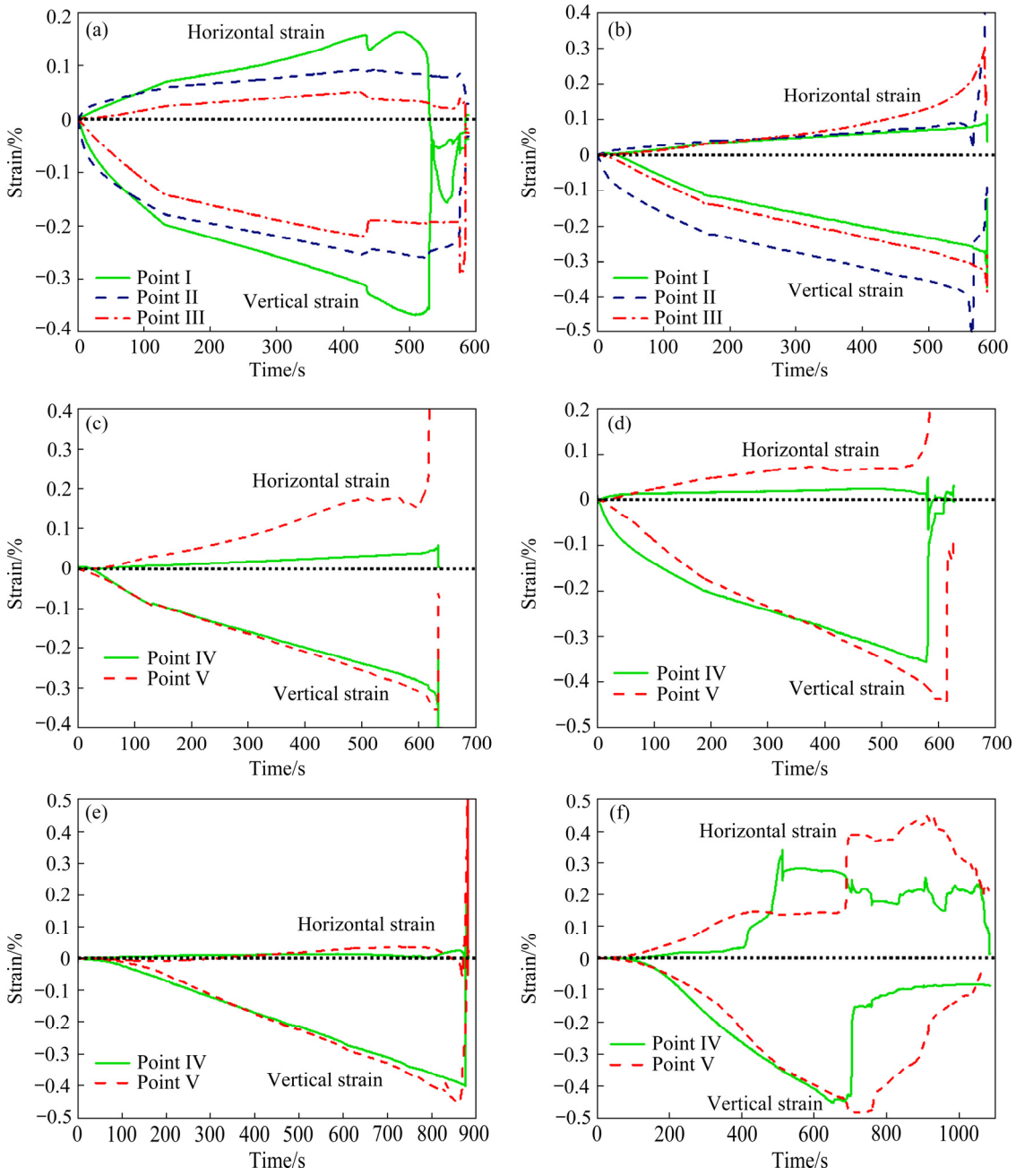

Fig. 8 Strain−time curves of specimens with different *H*/*W* ratios: (a) Specimen A1 (*H*/*W*=2.0); (b) Specimen B1 (*H*/*W*=1.0); (c) Specimen C1 (*H*/*W*=0.75); (d) Specimen D3 (*H*/*W*=0.50); (e) Specimen E4 (*H*/*W*=0.35); (f) Specimen F4 (*H*/*W*=0.20)

Point II (the front surface along the width) are greater than those at monitoring Point III (the side surface along with the thickness) and reach the first peak. For specimens with a *H*/*W* ratio less than 1.0, the strain at Point IV (the front surface along the width) gradually decreases with a decrease in the *H*/*W* ratio, eventually to a value less than that of monitoring Point V (the side surface along with the thickness), indicating that the failure of specimens with a high *H*/*W* ratio starts from the front surface along the width, whereas specimens with a *H*/*W* ratio less than 1.0 begin to break from the side surface along the thickness.

Combined with the specimen failure modes and strain–time curves, it is found that for specimens with *H*/*W* ratios ≥1.0, shear failure is dominant, and the shear fracture first appears on the side surface of the specimen. However, as the *H*/*W* ratio decreases, the tendency toward slabbing failure becomes obvious. The failure surface of

slabbing is approximately perpendicular to the side of the specimen, and the slabbing fractures first appear on the side surface. Monitoring point V (on the side surface) has a large strain value and reaches the first peak.

4.3 Influence of *H*/*W* ratio on acoustic emission

It is known that there are two types of rock fracture modes: tensile and shear. SHIOTANI et al [44] reported that tensile fracture and shear fracture could be distinguished by analyzing the rise time amplitude (RA) of AE signals during the fracture process. For rock materials, the RA value is often combined with the average frequency (AF) value to distinguish the fracture type [45]. The values of RA and AF for the AE signal can be expressed as

$$\mathrm{RA}=t/A_{\max},\quad \mathrm{AF}=N_{\mathrm{AE}}/t_{\mathrm{d}}$$

where t is the rise time, $A_{\max}$ is the maximum amplitude, N_{AE} is the AE ringdown-count, and t_{d} is the duration time.

Tensile fracture is generated by the extension of the original defect (fracture) at the fracture tip under the action of tensile stress, resulting in a short rise time and a high-frequency AE waveform. The development of shear fracture is the opposite, inducing an AE waveform with a long rise time and a low frequency. Thus, tensile fracture is characterized by low RA values and high AF values, and shear fracture is characterized by high RA values and low AF values, as shown in Fig. 9.

Figure 10 shows the RA–AF relationships of six typical specimens with different *H*/*W* ratios during uniaxial compression tests. For specimens with *H*/*W* ratios of 2.0, 1.0, 0.75, and 0.50, the AE data are clustered near the RA-axis; the AE signals of the specimens are characterized by high RA values and low AF values. Thus, the shear fracture is the main fracture that develops during the failure process of high *H*/*W* specimens. Moreover, with a decrease in the *H*/*W* ratio, the RA value of the AE signal gradually decreases, indicating an increasing number of tensile fractures in the failure process. Thus, with a decrease in the *H*/*W* ratio, slabbing failure gradually develops, and the failure mode changes from shear failure to shear–slabbing mixed failure, as shown in Figs. 10(c) and (d). For specimens with *H*/*W* ratios of 0.35 and 0.20 (Figs. 10(e) and (f)), the AE data are clustered near the AF-axis; the AE signals of the specimens are characterized by low RA values and high AF values. Thus, the tensile fracture is the main fracture that develops during the failure process of low *H*/*W* specimens.

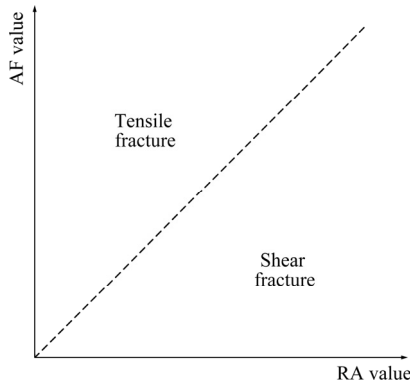

Fig. 9 Relationship among fracture type and RA value and AF value

Based on the experimental results, it is confirmed that slabbing failure is a special type of tensile failure. The RA results for low *H*/*W* specimens show typical tensile characteristics (low RA values and high AF values) that are similar to the experimental results of the Brazilian split test. Shear fractures rarely occur during the entire slabbing failure process, and specimens do not undergo the shear failure process. However, the failure process of shear–slabbing mixed failure is based mainly on the propagation of shear fractures. Thus, compared with shear failure and shear–slabbing mixed failure, the mechanism of slabbing failure is fundamentally changed.

4.4 Failure mechanism

According to the experimental results, tensile failure (slabbing failure) occurs during the failure process of specimens with *H*/*W* ratios less than 0.50 in uniaxial compression tests. In this section, the cause and mechanism of slabbing failure in uniaxial compression tests are discussed from the perspective of fracture propagation.

It is known that a natural rock mass is a heterogeneous material and usually contains a large number of randomly distributed micro-fractures. Some researchers have simulated micro-fractures in rock materials by adding artificial pre-fractures in the specimens and performing uniaxial compression tests on pre-fracture rock specimens to study the micro-fracture propagation law. WONG and EINSTEIN [46], and ZHU et al [47] summarized

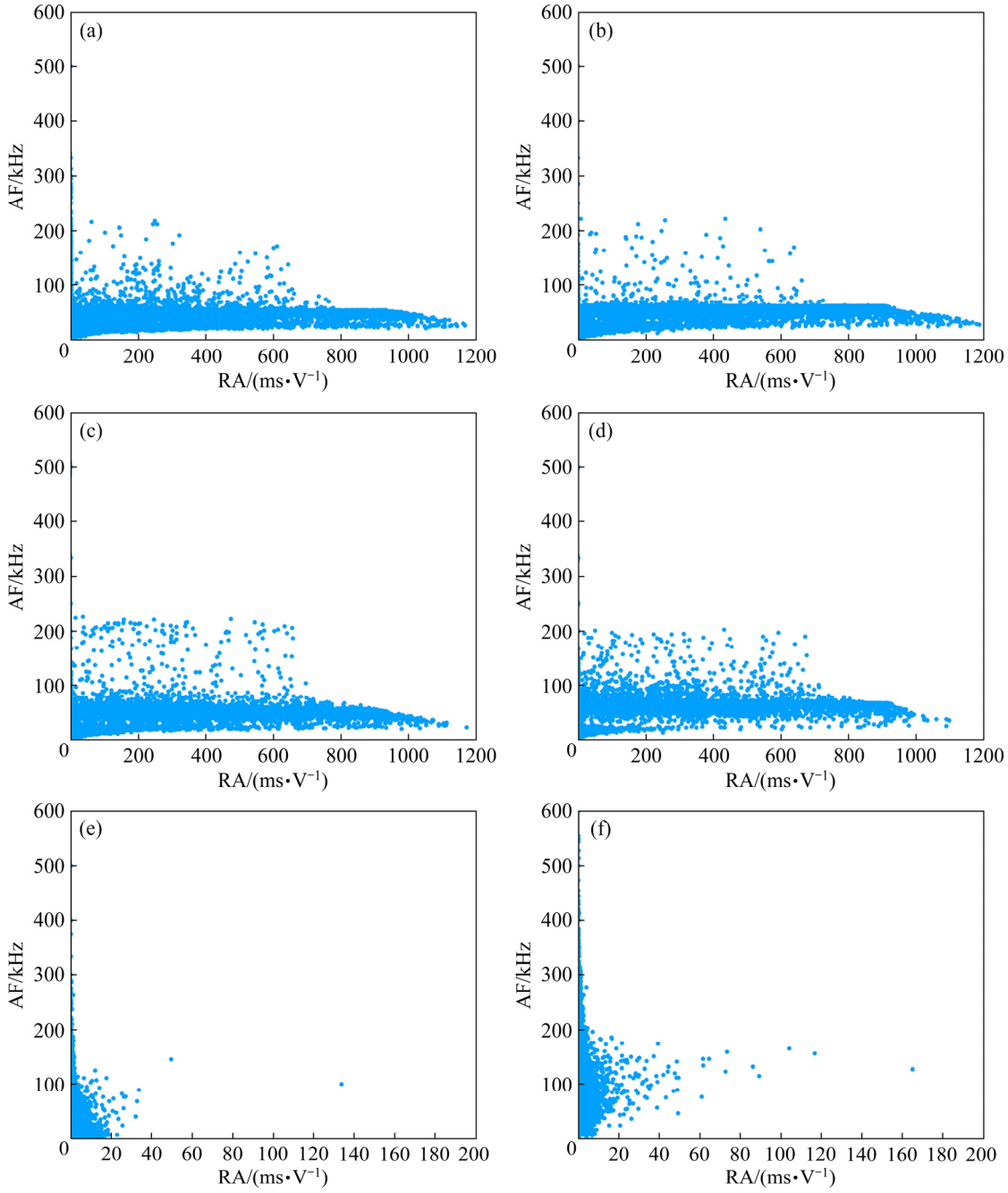

Fig. 10 Relationships between AF versus RA for specimens with different *H*/*W* ratios: (a) Specimen A3 (*H*/*W*)=2.0; (b) Specimen B2 (*H*/*W*)=1.0; (c) Specimen C3 (*H*/*W*)=0.75; (d) Specimen D2 (*H*/*W*)=0.50; (e) Specimen E4 (*H*/*W*)=0.35; (f) Specimen F4 (*H*/*W*)=0.20

seven fracture propagation models for pre-fracture specimens under uniaxial compression. It was found that fracture propagation always manifests in two stages: the tensile wing fracture propagation stage and the shear secondary fracture propagation stage.

Based on the fracture propagation law for pre-fracture specimens, the failure mechanism of intact rock specimens containing randomly distributed micro-fractures can be further deduced. As shown in Fig. 11(a), the micro-fractures of the prism granite specimens underwent two fracture propagation stages in the failure process. For specimens controlled by shear fracture, tensile wing fractures appeared at the end of the micro-fractures and extended. The fracture extension direction gradually paralleled the loading direction. At this stage, the specimen began to enter the plastic phase,

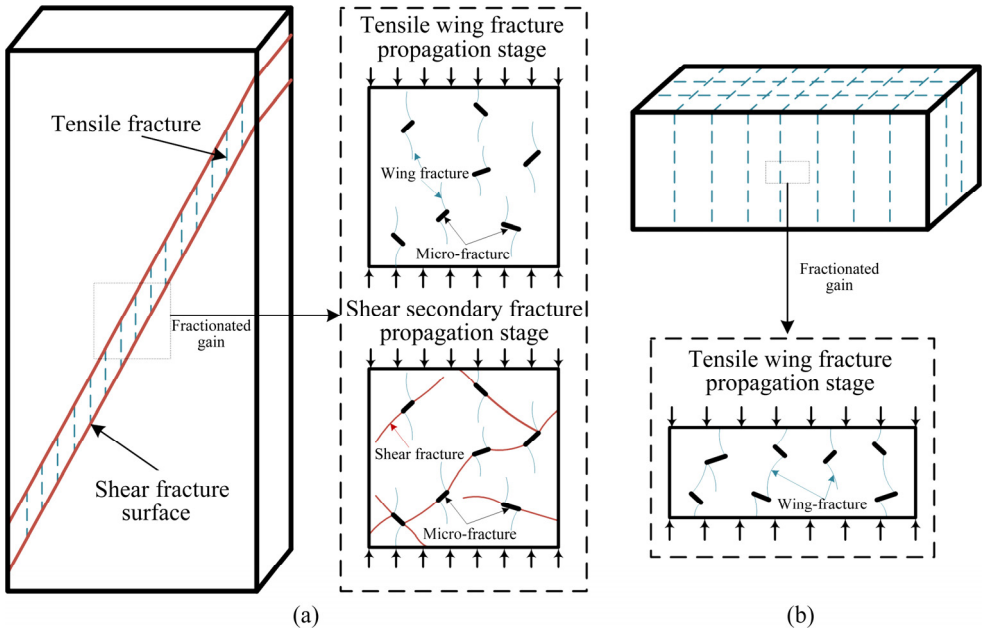

Fig. 11 Schematic diagrams of failure mechanisms in two different fracture modes: (a) Shear fracture; (b) Slabbing fracture

and the RA value of the AE signal showed tensile characteristics. The extension of tensile wing fracture reached its limit and stopped, and the specimen entered the shear secondary fracture propagation stage. Secondary shear fractures continued to extend, penetrating the specimen as loading continued. Complete shear failure surfaces were eventually formed, leading to shear failure.

As shown in Fig. 11(b), for specimens controlled by slabbing fracture, the fracture expansion law is significantly different from that for shear failure due to the geometric shape of the specimen. For specimens with a low H/W ratio, the expanding micro-fractures are only tensile wing fractures. Since the specimen is very short along the fracture extending direction, the extension of the tensile wing fracture is sufficient to cause the failure of the entire specimen. The expansion of secondary shear fractures does not have a chance to occur. With the expansion and connection of the tensile wing fracture, a series of tensile failure surfaces parallel to the loading direction were formed, causing slabbing failure. A specimen with lower H/W ratio is more conducive to forming a tensile failure surface caused by tensile wing fractures, which is more likely slabbing failure.

According to the mechanism analysis of slabbing failure, the experimental results in this study can be explained as follows.

(1) The large decrease in UCS in specimens with H/W ratios less than 0.50 (Fig. 7) is due to a fundamental change in the failure mode from shear failure to tensile (slabbing) failure.

(2) Specimens that experience slabbing failure have long yield platforms which have significant oscillations in their stress−strain curves (Fig. 4). Their UCS values are more discrete (Fig. 7) because the extension direction of the tensile wing fracture and tensile failure surface always tends to be parallel to the loading direction, resulting in specimens with an unstable load-carrying capacity after slabbing failure surfaces have been formed.

(3) The RA−AF diagrams of the AE signals in Groups E and F are significantly different from those in Groups A, B, C and D (Fig. 10), which is caused by the special failure mechanism of slabbing. Tensile wing fractures and secondary shear fractures have different chronological orders during the propagation of micro-fractures. For the specimens in Groups E and F, the failure mode is slabbing developed from tensile wing fracture. Micro-fracture extension stops at the tensile wing fracture extension stage, and secondary shear fracture does not occur. Thus, only the AE signals of tensile wing fractures can be detected, and the RA−AF characteristics of the specimens only show tensile fracture ones. On the contrary, the failure modes of specimens in Groups A, B, C and D are

shear failure or shear–slabbing mixed failure generated from both tensile wing fractures and secondary shear fractures. Both AE signals in tensile and shear fractures are indicated. However, the RA−AF behavior finally presented is shearing, which is the characteristic of the secondary shear fractures dominating and causing eventual failure of the specimen.

5 Conclusions

(1) For specimens with *H*/*W* ratios greater than 0.50, the UCS of the specimen increases gradually with a decrease in the *H*/*W* ratio; while for specimens with *H*/*W* ratios less than 0.50, the UCS decreases with a decrease in the *H*/*W* ratio.

(2) The stress−strain curves of specimens with different *H*/*W* ratios have significant differences in the peak plastic phase. For specimens with *H*/*W* ratios greater than or equal to 1.0, the stress−strain curves do not fluctuate significantly at the peak phase; for specimens with *H*/*W* ratios less than 1.0, the stress−strain curves exhibit long yield platforms with significant oscillations.

(3) For specimens with *H*/*W* ratios greater than 0.50, the failure changes from shear mode to shear–slabbing mixed mode with a decrease in *H*/*W* ratio, and the AE signals indicate shear fracture characteristics. For specimens with *H*/*W* ratios less than 0.50, the failures are controlled by the slabbing mode, with AE signals indicating tensile fracture characteristics.

(4) For specimens with low *H*/*W* ratios, slabbing failure is caused by the extension of tensile wing fractures. In practical application, short pillars with low *H*/*W* ratios should be avoided, especially in fractured rock masses. The strength design of short pillars and low *H*/*W* ratio rock structures should consider the impact of slabbing failure and use appropriate strength reduction to ensure rock mass stability and engineering safety.

Acknowledgments

The authors are grateful for the financial support from the National Natural Science Foundation of China (Nos. 11972378, 51904335, 51927808), and the Fundamental Research Funds for the Central Universities of Central South University, China (No. 2021zzts0282).

References

[1] LI Xi-bing, YAO Jin-rui, GONG Feng-qiang. Dynamic problems in deep exploitation of hard rock metal mines [J]. The Chinese Journal of Nonferrous Metals, 2011, 21(10): 2551−2563. (in Chinese)

[2] HOU Zheng-meng. Mechanical and hydraulic behavior of rock salt in the excavation disturbed zone around underground facilities [J]. International Journal of Rock Mechanics and Mining Sciences, 2003, 40(5): 725−738.

[3] LI Xi-bing, CHEN Zheng-hong, WENG Lei, LI Chong-jin. Unloading responses of pre-flawed rock specimens under different unloading rates [J]. Transactions of Nonferrous Metals Society of China, 2019, 29(7): 1516−1526.

[4] LONG Yi, LIU Jian-po, LEI Gang, SI Ying-tao, ZHANG Chang-yin, WEI Deng-cheng, SHI Hong-xu. Progressive fracture processes around tunnel triggered by blast disturbances under biaxial compression with different lateral pressure coefficients [J]. Transactions of Nonferrous Metals Society of China, 2020, 30(9): 2518−2535.

[5] BEHERA B, YADAV A, SINGH G S P, SHARMA S K. A numerical modeling approach for evaluation of spalling associated face instability in longwall workings under massive sandstone roof [J]. Engineering Failure Analysis, 2020, 117: 104927.

[6] FAIRHURST C, COOK N G W. The maximum phenomenon of rock splitting parallel to the direction compression in the neighbourhood of a surface [C]//Proceedings of the 1st ISRM Congress. Lisbon: OnePetro, 1966.

[7] ORTLEPP W D. Rock fracture and rockbursts: An illustrative study [M]. Johannesburg: South African Institute of Mining and Metallurgy, 1997.

[8] CAI Ming. Influence of intermediate principal stress on rock fracturing and strength near excavation boundaries—Insight from numerical modeling [J]. International Journal of Rock Mechanics and Mining Sciences, 2008, 45(5): 763−772.

[9] EXADAKTYLOS G E, TSOUTRELIS C E. Pillar failure by axial splitting in brittle rocks [J]. International Journal of Rock Mechanics and Mining Sciences & Geomechanics Abstracts, 1995, 32(6): 551−562.

[10] MARTIN C D, MAYBEE W G. The strength of hard-rock pillars [J]. International Journal of Rock Mechanics and Mining Sciences, 2000, 37(8): 1239−1246.

[11] DU Kun, LI Xi-bing, LI Di-yuan, WENG Lei. Failure properties of rocks in true triaxial unloading compressive test [J]. Transactions of Nonferrous Metals Society of China, 2015, 25(2): 571−581.

[12] WAWERSIK W R, FAIRHURST C. A study of brittle rock fracture in laboratory compression experiments [J]. International Journal of Rock Mechanics and Mining Sciences & Geomechanics Abstracts, 1970, 7(5): 561−575.

[13] HOLZHAUSEN G R, JOHNSON A M. Analyses of longitudinal splitting of uniaxially compressed rock cylinders [C]//International Journal of Rock Mechanics and Mining Sciences & Geomechanics Abstracts, 1979, 16(3): 163−177.

[14] HORII H, NEMAT-NASSER S. Compression-induced microcrack growth in brittle solids: Axial splitting and shear

failure [J]. Journal of Geophysical Research: Solid Earth, 1985, 90(B4): 3105−3125.

[15] FREDDI F, ROYER-CARFAGNI G. Variational fracture mechanics to model compressive splitting of masonry-like materials [J]. Annals of Solid and Structural Mechanics, 2011, 2(2/3/4): 57−67.

[16] LI D Y, LI C C, LI X B. Influence of sample height-to-width ratios on failure mode for rectangular prism samples of hard rock loaded in uniaxial compression [J]. Rock Mechanics and Rock Engineering, 2011, 44(3): 253−267.

[17] FENG Fan, LI Xi-bing, LI Di-yuan. Modeling of failure characteristics of rectangular hard rock influenced by sample height-to-width ratios: A finite/discrete element approach [J]. Comptes Rendus Mécanique, 2017, 345(5): 317−328.

[18] HUDSON J A. Effect of time on the mechanical behaviour of failed rock [J]. Nature, 1971, 232(5307): 185−186.

[19] DAS M N. Influence of width/height ratio on post-failure behaviour of coal [J]. International Journal of Mining and Geological Engineering, 1986, 4(1): 79−87.

[20] YANG Sheng-qi, XU Wei-ya, SU Cheng-dong. Study on statistical damage constitutive model of rock considering scale effect [J]. Chinese Journal of Rock Mechanics and Engineering, 2005, 24(24): 4484−4490. (in Chinese)

[21] DIRIGE A P, ARCHIBALD J. The effects of geometry on the uniaxial compressive strength properties of intact rock core specimens [C]//Proceedings of the 41st US Symposium on Rock Mechanics (USRMS). Golden: OnePetro, 2006.

[22] MASOUMI H, BAHAADDINI M, KIM G, HAGAN P. Experimental investigation into the mechanical behavior of Gosford sandstone at different sizes [C]//Proceedings of the 48th US Rock Mechanics/Geomechanics Symposium. Minneapdis: OnePetro, 2014.

[23] ZHAO Xing-guang, CAI Ming, WANG Ju, LI Peng-fei. Strength comparison between cylindrical and prism specimens of Beishan granite under uniaxial compression [J]. International Journal of Rock Mechanics and Mining Sciences, 2015, 76: 10−17.

[24] GÜNEYLI H, RÜŞEN T. Effect of length- to-diameter ratio on the unconfined compressive strength of cohesive soil specimens [J]. Bulletin of Engineering Geology and the Environment, 2016, 75(2): 793−806.

[25] PENG J, WONG L N Y, TEH C I. A re-examination of slenderness ratio effect on rock strength: Insights from DEM grain-based modelling [J]. Engineering Geology, 2018, 246: 245−254.

[26] THURO K, PLINNINGER R J, ZäH S, SCHüTZ S. Scale effects in rock strength properties. Part 1: Unconfined compressive test and Brazilian test [C]//ISRM Regional Symposium. Espoo: EUROCK, 2001.

[27] WEN Zhi-jie, WANG Xiao, CHEN Lian-jun, LIN Guan, ZHANG Hua-lei. Size effect on acoustic emission characteristics of coal-rock damage evolution [J]. Advances in Materials Science and Engineering, 2017, 2017: 1−8.

[28] TANG Chun-an, THAM L G, LEE P K K, TSUI Y, LIU Hong. Numerical studies of the influence of microstructure on rock failure in uniaxial compression—Part II: Constraint, slenderness and size effect [J]. International Journal of Rock Mechanics and Mining Sciences, 2000, 37(4): 571−583.

[29] XU Yu-hang, CAI Ming. Numerical simulation of end constraint effect on post-peak behaviors of rocks in uniaxial compression [C]//The 49th US Rock Mechanics/ Geomechanics Symposium. San Francisco: OnePetro, 2015.

[30] LIANG C Y, ZHANG Q B, LI X, XIN P. The effect of specimen shape and strain rate on uniaxial compressive behavior of rock material [J]. Bulletin of Engineering Geology and the Environment, 2016, 75(4): 1669−1681.

[31] CARPINTERI A, CORNETTI P, PUZZI S. Size effect upon grained materials tensile strength: The increase of the statistical dispersion at the smaller scales [J]. Theoretical and Applied Fracture Mechanics, 2005, 44(2): 192−199.

[32] DARLINGTON W J, RANJITH P G, CHOI S K. The effect of specimen size on strength and other properties in laboratory testing of rock and rock-like cementitious brittle materials [J]. Rock Mechanics and Rock Engineering, 2011, 44(5): 513−529.

[33] LIU Huai-zhong, LIN Jeen-shang, HE Jiang-da, XIE Hong-qiang. Discrete elements and size effects [J]. Engineering Fracture Mechanics, 2018, 189: 246−272.

[34] GUO Yi-de, HUANG Lin-qi, LI Xi-bing, CHEN jiang-zhan, SUN Jing-nan. Experimental investigation on the effects of thermal treatment on the physical and mechanical properties of shale [J]. Journal of Natural Gas Science and Engineering, 2020, 82: 103496.

[35] BRADY B H G, BROWN E T. Rock mechanics: For underground mining [M]. Berlin: Springer, 1993.

[36] HOEK E, BROWN E T. Practical estimates of rock mass strength [J]. International Journal of Rock Mechanics and Mining Sciences, 1997, 34(8): 1165−1186.

[37] DRUCKER D C, PRAGER W. Soil mechanics and plastic analysis or limit design [J]. Quarterly of Applied Mathematics, 1952, 10(2): 157−165.

[38] MOGI K. Experimental rock mechanics [M]. New York: CRC Press, 2006.

[39] WIEBOLS G A, COOK N G W. An energy criterion for the strength of rock in polyaxial compression [J]. International Journal of Rock Mechanics and Mining Sciences & Geomechanics Abstracts, 1968, 5(6): 529−549.

[40] LI Chun-lin. Micromechanics modelling for stress–strain behaviour of brittle rocks [J]. International Journal for Numerical and Analytical Methods in Geomechanics, 1995, 19(5): 331−344.

[41] WONG R H C, LIN P, TANG C A. Experimental and numerical study on splitting failure of brittle solids containing single pore under uniaxial compression [J]. Mechanics of Materials, 2006, 38(1/2): 142−159.

[42] TUNCAY E, HASANCEBI N. The effect of length to diameter ratio of test specimens on the uniaxial compressive strength of rock [J]. Bulletin of Engineering Geology and the Environment, 2009, 68(4): 491−497.

[43] WANG Shao-feng, LI Xi-bing, DU Kun, WANG Shan-yong, TAO Ming. Experimental study of the triaxial strength properties of hollow cylindrical granite specimens under coupled external and internal confining stresses [J]. Rock Mechanics and Rock Engineering, 2018, 51(7): 2015−2031.

[44] SHIOTANI T, OHTSU M, IKEDA K. Detection and evaluation of AE waves due to rock deformation [J]. Construction and Building Materials, 2001, 15(5/6): 235−246.

[45] WANG Hong-jian, LIU Da-an, CUI Zhen-dong, CHENG Cheng, JIAN Zhou. Investigation of the fracture modes of red sandstone using XFEM and acoustic emissions [J]. Theoretical and Applied Fracture Mechanics, 2016, 85: 283−293.
[46] WONG L N Y, EINSTEIN H H. Systematic evaluation of cracking behavior in specimens containing single flaws under uniaxial compression [J]. International Journal of Rock Mechanics and Mining Sciences, 2009, 46(2): 239−249.
[47] ZHU Quan-qi, LI Di-yuan, LI Xi-bing. Experimental study on failure and mechanical characteristics of marble containing a prefabricated elliptical hole [J]. Chinese Journal of Rock Mechanics and Engineering, 2019, 38(S1): 2724−2733. (in Chinese)

单轴压缩作用下不同高宽比硬岩试样的破坏模式与板裂破坏机理

赵宇喆[1]，黄麟淇[1]，李夕兵[1]，黎崇金[1]，陈正红[2]，曹芝维[1]

1. 中南大学 资源与安全工程学院，长沙 410083；
2. 湖南科技大学 土木工程学院，湘潭 411201

摘　要：为了研究板裂破坏与试件高宽比(*H*/*W*)之间的关系以及板裂破坏的发生条件、破坏特征和力学机理，对 6 组花岗岩试样进行单轴压缩试验。利用应变监测仪和高速摄影仪记录试样的破坏全过程，通过分析应力、应变以及声发射的监测结果确定裂纹的发生和扩展路径。结果表明，*H*/*W* 的变化可以改变试样的宏观破坏模式。当 *H*/*W* 降低至 0.5 时，试样破坏模式以板裂破坏为主；板裂破坏发生时试样承载力降低，裂纹拓展方向近似平行于加载方向。此外，发生板裂破坏的试样的裂纹扩展过程和声发射信号均呈典型拉伸破坏特征，表明板裂破坏本质上是一种特殊的拉伸破坏。

关键词：硬岩；破坏模式；板裂破坏；声发射；拉伸翼裂纹

(Edited by Wei-ping CHEN)